

Electronic Supplementary Information

X-ray propagation imaging of a lipid bilayer in solution

André Beerlink^{*a,b}, Shashi Thutupalli^c, Michael Mell^{b,d}, Matthias Bartels^b, Peter Cloetens^e,
Stephan Herminghaus^c, and Tim Salditt^{*b}

^a *Current address: Deutsches Elektronen-Synchrotron, Notkestraße 85, 22605 Hamburg, Germany. Tel: +49(0)40 8998 1985; Fax: +49(0)40 8994 1985; E-mail: andre.beerlink@desy.de*

^b *Institut für Röntgenphysik, Georg-August-Universität Göttingen, Friedrich-Hund-Platz 1, 37077 Göttingen, Germany. E-mail: tsalditt@gwdg.de*

^c *Max-Planck-Institute for Dynamics and Self-Organization, Am Faßberg 17, 37077 Göttingen, Germany.*

^d *Current address: Mechanics of Biological Membranes and Biorheology, Departamento de Química Física I, Universidad Complutense, 28040 Madrid, Spain.*

^e *European Synchrotron Radiation Facility, 6 Rue Jules Horowitz, 38043 Grenoble Cedex, France.*

1 Membrane preparation

1.1 Preparation of Black Lipid Membranes (BLMs)

The preparation of planar free-standing, solvent-containing lipid membranes goes back to the work of Müller and Rudin^{1,2}. Although the remaining organic solvent in this kind of reconstituted membranes might be considered problematic, the preparation is very fast and yields more stable bilayers compared to the preparation of Montal and Müller³. Therefore, we have mainly used this approach in our initial study of BLMs in synchrotron beams. In detail, the membranes were prepared as described previously^{4,5}. Teflon foils and “functionalized” silicon substrates are homogeneously pre-treated with Loctite Primer 770 (Henkel; Germany), which has an additional hydrophobizing effect on the surface. Afterwards the substrates are glued to a Teflon wall dividing two compartments inside the experimental chamber (see figure S1) using Loctite 406 (Henkel; Germany). A solution of the phospholipid diphytanoylphosphatidylcholine (DPhyPC, Avanti Lipids; Alabaster, USA) dissolved in methanol (10 mg/mL) is painted across the substrate surface, using a thinned, natural hair paintbrush. This serves as an additional anchor layer for the final membrane; inhomogeneous lipid layers are formed at the surface as the solvent evaporates. Subsequently the chamber is filled with buffer solution (150 mM NaCl, 5 mM Hepes, pH 7.0 NaOH). The membrane is “painted” with another paint brush from a lipid solution (DPhyPC/decane, 20 mg/mL). The membrane capacitance is recorded by using a modified Port-a-Patch NPC-1 system (Nanion; Germany), equipped with an EPC-10 amplifier (HEKA;

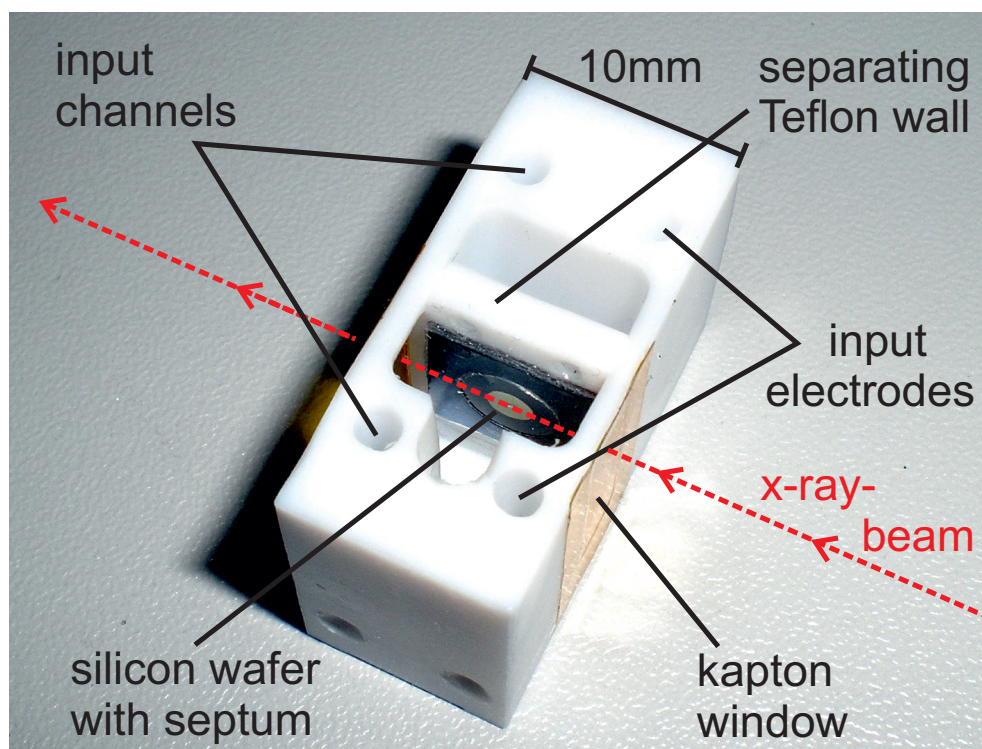


Fig. S1 Image of chamber for BLM imaging. The structured Teflon foil is glued to the Teflon wall separating two aqueous compartments. Hydrostatic pressure and electric potentials across the membrane are controlled via two holes for tubings and electrodes connected to each compartment.

Germany). The signal is transduced into both compartments of the measurement chamber by Ag/AgCl-electrodes (see figure S1). The membrane immediately starts to thin and after approximately 15 minutes, depending on the amount of solvent initially present in the membrane, a pure lipid bilayer remains and shows a characteristic charging and discharging peak in the current response. Subsequently, the specific capacitance can be calculated. A BLM on a 200 μm hole gives a typical capacitance value of 150 pF corresponding to $c_m = 0.48 \frac{\mu\text{F}}{\text{cm}^2}$, which is in perfect agreement with known literature values². For the synchrotron experiments an additional shielding around the chamber was mounted to the sample stage to suppress electrical noise originating from various sources in the experimental hutch at the beamline.

1.2 Preparation of microfluidic BLMs (mfBLMs)

A detailed description of the preparation of microfluidic chips, see figure S2(a) themselves, which are used for mfBLM formation, can be found in previous literature^{6,7}. Different window materials, e.g. Polypropylene, Polyimide (kapton), silicon nitride, Ultralene, etc., can be chosen here as shown in figure S2(b). However, to simplify matters a self-adhesive kapton foil (Dr. D. Müller GmbH; Ahlhorn, Germany) of 25 μm thickness is used. The MF chip is placed on the window material, which is subsequently cut to fit the size of the chip. Nanoports N333 (10-32 for 1/16" tubing, BESTA-Technik GmbH; Wilhelmsfeld, Germany) are glued to the kapton at the end of the channels, see figure S2(c). Drying is at 120°C for 1 h with the application of

weight pressure. The sealed hole is widely opened with a hot needle to avoid blockage of the channels. Now the second window is bound to the other side of the MF chip. PTFE tubing (Novodirect; Kehl, Germany) with inner and outer diameter of 0.5 mm and 1.6 mm runs in the fitting (F333) and the ferrule (F142) and is connected to the fixed Nanoport (figure S2(c)). At the

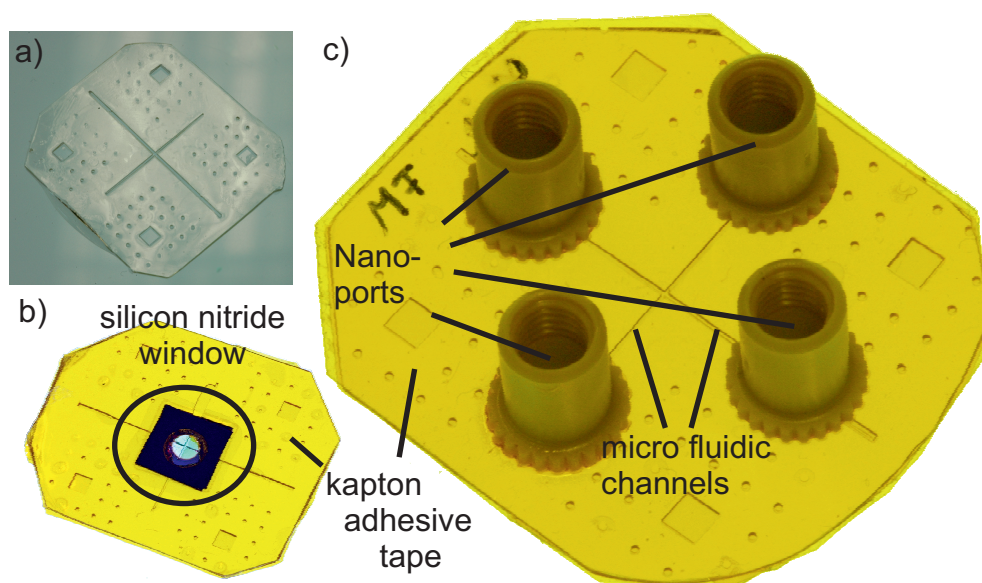


Fig. S2 The photograph shows (a) the UV glue microfluidic chip after it is cured. (b) The window material, here a 150 nm silicon nitride window, is placed at the channel cross and the device is sealed with self-adhesive kapton tape. (c) Nanoports are glued at the channel entrances for application of tubings and syringes. The microfluidic devices which were made from eroded metal plates are not depicted.

other end of the tubings a Hamilton syringe (Schütt; Germany) is connected. Volumes of 0.5 mL or 1 mL for aqueous buffer and 0.25 mL or 0.5 mL for the lipid solutions are used. Deionized and distilled water (MilliQ (MQ), Millipore; Germany) or buffer solutions with 150 mM NaCl (pH=7) is used for the preparation. The oil solutions consist of either DPhyPC in n-decane (see BLM formation) or Monoolein (Avanti Lipids; Alabaster, USA) in Squalene (Merk; Germany), both at a concentration of 10 mg/mL. The syringes are mounted onto a self-made pump system that is controlled by a LabView GUI (National Instruments) allowing injection speeds to be precisely controlled, up to volumes of 500 $\mu\text{L}/\text{h}$. The membranes are prepared by running the oil pump for approximately 10 minutes to flush the channels with the lipid solution. This procedure has an additional hydrophobizing effect helping to promote the formation of convex water interfaces (also called “water fingers” (see figure S3(a)). Subsequently, the oil flow is stopped and the water fingers are slowly brought into contact in the channel cross region. When the two monolayers are brought together, intense Fresnel fringes appear in the visible light microscope (figure S3(b)). Due to a stochastic instability the monolayers suddenly fuse, the surrounding oil is expelled to the Plateau-Gibbs border and the Black Lipid Membrane forms as described previously (figure S3(c)). The size of the bilayer patch can be controlled by variation of the pressure in the water channels. The presence of a single bilayer can be checked by capacitance measurements or by comparison of the fresnel fringes in the regions of the two monolayers and the single bilayer (see figure S3(c,d)).

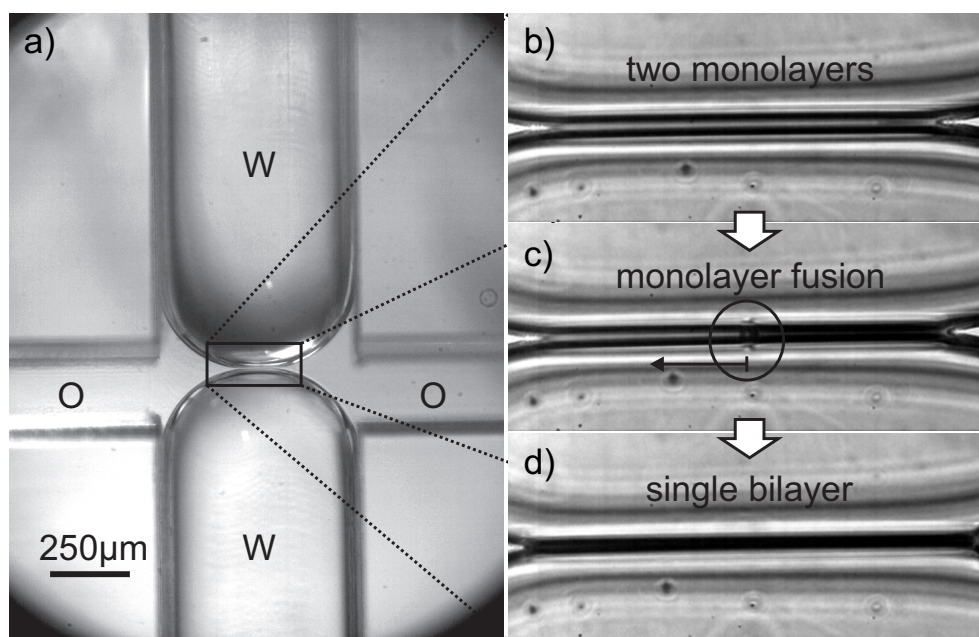


Fig. S3 Formation of a mfBLM in a microfluidic device. a) Bright field microscopy image of two “water fingers” (W). They are exposed to a oily squalene-Monoolein solution (O) and brought into contact at the channel crossing. Phase contrast light microscopy series: b) Zoom-in of the approaching monolayers. c) Local instabilities initiate the monolayer fusion until a bimolecular membrane (mfBLM) is left (d).

2 Fitting model

According to the sample symmetry, the data analysis process is reduced to a one-dimensional problem. Data reduction for parallel beam imaging (plane wave illumination) has already been described in detail in a former work⁵ (supporting online material). The present work is a generalization, since by use of the Fresnel scaling theorem, the spherical (quasi-point source) illumination can be reduced to the parallel beam case, after a suitable coordinate transformation, see below. Let us therefor briefly reiterate image formation in the parallel beam case, where the measured intensity profile $I(x, z)$ can be considered as the defocus (propagation based) image of the object. The measured $I(x, z)$ can be treated as the output of an operator describing the image formation, and acting on the one-dimensional complex-valued optical transmission function $T(x) = A(x) \cdot e^{i\varphi(x)}$, as an input. $T(x)$ reflects the structure of the membrane patch along its local normal axis in the object plane, after a local average in the (lateral) tangent plane of the membrane. The accumulated phase shift difference with respect to the empty space of the wave traversing the membrane is $\varphi(x) = -k \int_L \delta(x, z) dz$, where $n = 1 - \delta$ is the real part of the index of refraction, $k = 2\pi/\lambda$ the wave number, and $L(x)$ the interaction length. This projection approximation is justified for hard x-rays and weakly scattering objects of the given size. Furthermore, absorption can be neglected and setting $A(x) = 1$, only phase contrast must be considered here. For simplicity, we first consider the simplest membrane structure with constant optical index (electron density), which is well suited for black lipid membranes swollen with organic solvent before the thinning transition takes place. The phase profile behind the object (exit wave) is then simply $\varphi(x) \simeq -k\Delta\delta L(x)$, with $\Delta\delta$ the refractive index difference

with respect to the surrounding water with $\Delta\delta < 0$. For the path length, simple geometry (see Fig. 2(a) in publication) yields

$$L(x) = \begin{cases} 2 \left(\sqrt{(R+d)^2 - x^2} - \sqrt{R^2 - x^2} \right), & \text{if } x \leq R \\ 2\sqrt{(R+d)^2 - x^2}, & \text{if } R < x \leq R+d \\ 0, & \text{if } x > R+d. \end{cases} \quad (1)$$

For further simplification we substitute $R' = \frac{R}{d}$ and $x' = \frac{x}{d}$. If we consider $R' \gg 1$ (i.e. $R \gg d$) we achieve a normalized path length

$$L_N(x') \approx 2 \cdot 2\sqrt{2R'+x'} \left[\sqrt{1-x'} - \sqrt{-x'} \right], x' \in [-R', 0]. \quad (2)$$

Because $|R'| \gg |x'|$ one gets $2\sqrt{2R'+x'} \approx 2\sqrt{2R'}$ that leads to

$$L_N(x') = 2 \cdot 2\sqrt{2Rd} \begin{cases} \sqrt{1-x'} - \sqrt{-x'}, & \text{if } R' \leq x' \leq 0 \\ \sqrt{1-x'}, & \text{if } 0 < x' \leq 1 \\ 0, & \text{if } x' > 1 \end{cases} \quad (3)$$

in units of membrane thicknesses d on the abscissa.

The image operator itself is given in paraxial approximation by the (1D) Fresnel-Kirchhoff equation,

$$E(x_d, z) = E_0 \sqrt{\frac{k}{2\pi z}} e^{-i\frac{\pi}{4}} \int_{-\infty}^{\infty} e^{i\varphi(x)} e^{\frac{ik(x-x_d)^2}{2z}} dx, \quad (4)$$

and $I(x, z) = |E(x, z)|^2$ for each propagation (defocus) distance z . For numerical computation of the Fresnel intensity profile $I(x, z)$, a simple box model of $\varphi(x)$ can be used for the central interval of the object plane $[x_{min}, x_{max}]$, where the phase shift $\varphi(x)$ is non-zero, see figure S4. The interval is divided into N segments of a constant phase shift $\Phi_j = \Phi(x_j)$, with $x_j = x_{min} + j\Delta$, with $K_j := T(x_{min} + j\Delta) = e^{i\Phi(x_{min} + j\Delta)}$. Using Fresnel Sine and Cosine functions, the field in the detector plane becomes

$$E_c(x) = \sum_{j=0}^{N-1} \frac{E_0 K_j}{\sqrt{2}} e^{-i\frac{\pi}{4}} \left[(C(w_{j+1}) - C(w_j)) + i(S(w_{j+1}) - S(w_j)) \right] \quad (5)$$

with $w_j = \sqrt{\frac{k}{\pi z}}(x_{min} + j\Delta - x_d)$. To obtain the complete field $E(x) = E_c(x) + E_l(x) + E_r(x)$, the fields $E_l(x)$ and $E_r(x)$ due to the source points in the left and right half-planes (bordering the object interval $[x_{min}, x_{max}]$ in the sample plane) have to be added. For these regions constant (in practice often zero) relative phase shift φ_l and φ_r can be assumed. For computational speed, the actual calculations of $I(x, z)$ during the least squares fitting were performed in trapezoidal approximation of the transmission function $T(x)$, where the phase $\varphi(x)$ in each segment was linearly approximated, and better accuracy could be obtained for given number of segments, see figure S4. For a segment from x_j to x_{j+1} the phase $\Phi(x)$ is linearly approximated by

$$\Phi_j^m = m_j x + b_j, \quad x \in [x_j, x_{j+1}] \quad (6)$$

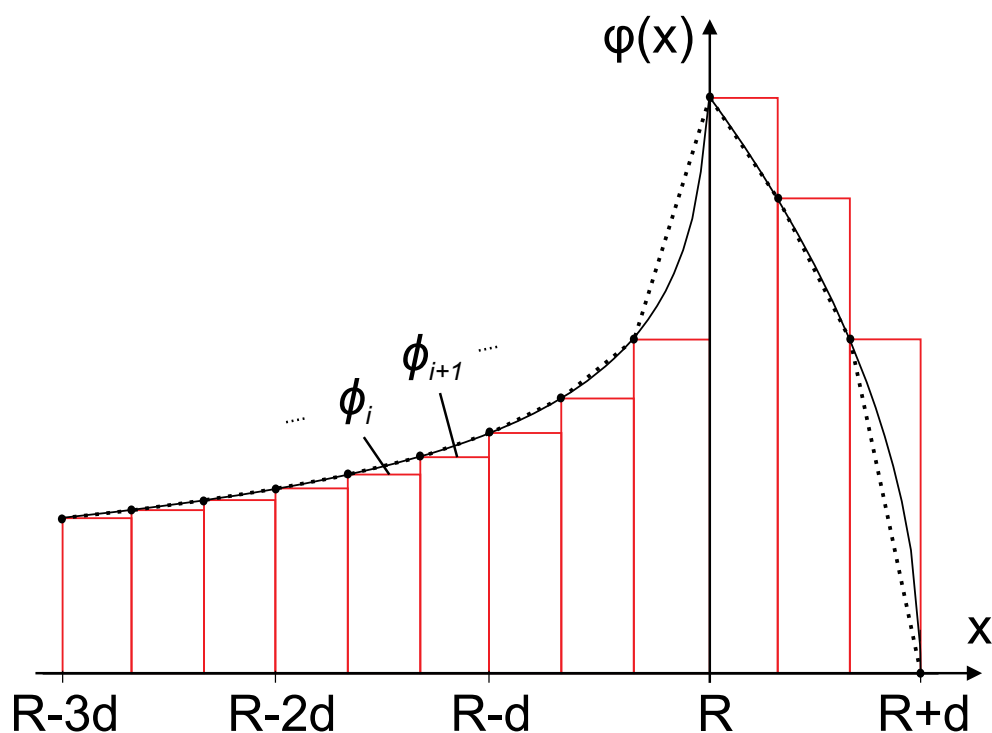


Fig. S4 The transmission function consisting of the phase $\varphi(x)$ (solid line) is sub-divided into N slabs of constant phase $\varphi(x_{min}) + j \cdot \Delta$ (red boxes). For computational speed, $\varphi(x)$ is modeled by a trapezoidal approximation (dashed line).

where $m_j = \frac{\Phi_{j+1} - \Phi_j}{x_{j+1} - x_j}$ and $b_j = \Phi_j - m_j x_j$. We can write a sum of Fresnel-Kirchhoff integrals for segments with a linear phase shift

$$E_c(x_d, z) = E_0 \sqrt{\frac{k}{2\pi z}} e^{-i\frac{\pi}{4}} \sum_{j=0}^{N-1} \int_{x_j}^{x_{j+1}} e^{i(m_j x + b_j)} e^{\frac{ik(x-x_d)^2}{2z}} dx. \quad (7)$$

The integrals over each segment can be calculated yielding

$$E_c(x_d, z) = \frac{E_0}{\sqrt{2}} \sum_{j=0}^{N-1} e^{i(b_j + m_j(x_d - \frac{m_j z}{k}))} \cdot [(C(w_{j+1}^T) - C(w_j^T)) + i(S(w_{j+1}^T) - S(w_j^T))] \quad (8)$$

with

$$w_j^T = \sqrt{\frac{k}{\pi z}} (x_j - x_d + \frac{m_j z}{k}). \quad (9)$$

3 Treatment of divergent beam illumination and simple examples (phase slit)

Next, the parallel beam analysis sketched out above has to be linked to the present experimental situation, where the object (sample) at z_1 from the source is illuminated by a divergent cone

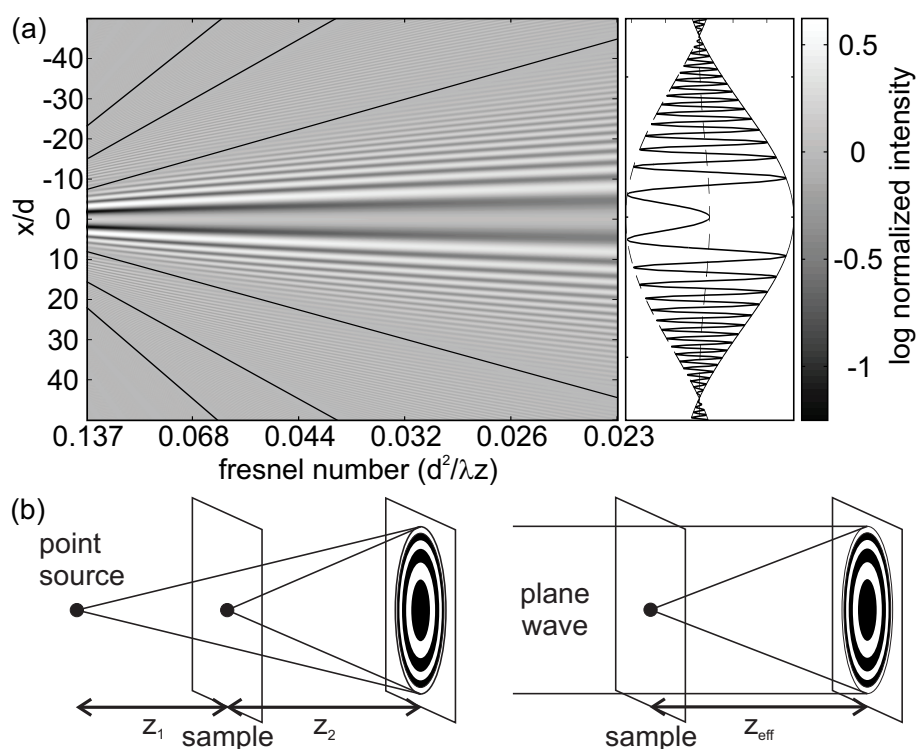


Fig. S5 (a) The logarithmic field intensity showing the evolution of the Fresnel diffraction pattern as the field propagates along z . The illustrative example of the simplest toy model corresponding to a symmetric phase slit of width $d = 2 \mu\text{m}$ and phase shift $\varphi = 2 \text{ rad}$ is shown for an x-ray energy of 17.5 keV . A representative intensity profile is plotted for a plane corresponding to a Fresnel number $F = 0.031$. The parabolic behavior of the oscillations is directly visible. The linear scaling of the sinc-functions produces bands that seem to radiate in a star-like manner from the left (indicated with black lines). These correspond to the nodes of the envelope functions. (b) According to the Fresnel scaling theorem, the diffraction image recorded with a point-source is equivalent to a magnified image of the wave field recorded with parallel beam illumination at an effective focal distance $z_{eff} = z_1 z_2 / (z_1 + z_2)$.

beam, and the detector is at z_2 from the sample. According to the so-called Fresnel scaling theorem for paraxial beams, free space propagation and the associated contrast formation is equivalent in the cone beam and parallel beam case, up to a simple coordinate transformation of the detector pixel size by the geometric magnification $M = (z_2 + z_1) / z_1$ and the defocus distance $z \rightarrow z_{eff}$ with an effective propagation distance $z_{eff} = z_1 z_2 / (z_1 + z_2)$ ⁸. It is this parallel beam equivalent coordinate system which is used for the present analysis.

The basic properties of the in-line phase contrast imaging approach as used here, including the scaling of resolution, contrast and the corresponding detection limits can be illustrated by considering the Fresnel diffraction downstream from a phase contrast slit. This can be understood as a transparent aperture in the sample plane with a single box phase profile, illuminated by (perfectly coherent) plane waves as shown in figure S5(a). The object is thus characterized by two parameters only, the slit width d and the phase shift φ . According to previous works by the authors^{9,10}, the Fresnel diffraction pattern as a function of distance x_d on the detector from

the optical axis and the propagation (defocus) distance z is given by

$$I(x_d) = E_0^2 \left[1 + d^2 \frac{k}{\pi z} (1 - \cos(\varphi)) \operatorname{sinc}^2\left(\frac{kx_d d}{2z}\right) - 2\sqrt{2}d \sqrt{\frac{k}{\pi z}} \sin\left(\frac{\varphi}{2}\right) \sin\left(\frac{kx_d^2}{2z} + \frac{\varphi}{2} + \frac{\pi}{4}\right) \operatorname{sinc}\left(\frac{kx_d d}{2z}\right) \right]. \quad (10)$$

For small contrast φ , the third term dominates the observable intensity profile as oscillatory signal around the mean (flat) primary beam intensity, enveloped by the far-field (Fraunhofer) form factor of a slit. The two parameters d and φ are independently encoded in the signal amplitude proportional to $d \sin(\varphi)$, and the phase shift of the oscillations with respect to the envelope. Importantly, the independent assessment of the two structural parameters is possible even if the numerical aperture of detection is smaller than λ/d , the resolution criterion for far-field diffraction. However, two necessary and sufficient conditions for resolving the phase slit are sizable contrast by lowering the defocus distance z , so that the ratio $\sqrt{d^2}/(\lambda z)$ is higher than the experimental detection limit, depending on flux density and on stability of the flat (empty beam) image. Thus in order to reach molecular length scales, z must be decreased. At the same time, a second important condition is that the detector pixels are small enough to allow proper sampling of the oscillatory signal along x_d , in particular as the spatial frequency is anti-proportional to λz , see figure S5(a). The fact that small z_{eff} can actually be realized experimentally by use of a focused beam as well as small (de-magnified) detector pixels, is exactly one of the main conclusions of the work. In summary, the above considerations show that an increased contrast / visibility of the Fresnel fringes can be reached by decreasing the propagation distance while at the same time a divergent beam is used to ensure a sufficient oversampling of the oscillations at the detector, see figure S5(b).

4 Inter-dependence of model parameters for the simple phase slit

Next, we discuss a second important issue: the inter-dependence of fitting parameters, i.e. to what extent the signal reflects all structural parameters. For a simple slit like object, according to equation 10, there are two main features in the fringe pattern: the amplitude and the phase of the oscillation with respect to the envelope. Note that the separations the minima depend primarily on the defocus and the wavelength. The amplitude scales with the product of the slit width and phase shift, and is thus not an independent measure of both parameters. For strong phase shifting samples, however, the oscillations begin to shift as a function of the object's phase, enabling a separate determination, lifting the parameter degeneracy. This issue is illustrated by simulation for different values of d and $\varphi \propto \Delta\delta$, shown in figure S6. As the results show, the present experimental parameters lead to a degeneracy, i.e. only the product of d and φ can be safely determined without a priori knowledge.

Experimentally, in future work one can increase φ to lift the degeneracy. For example decreasing the photon energy by a factor of three, $\Delta\delta$ will increase by about one order of magnitude. For a membrane of thickness in the range from 10 nm to 20 nm, the oscillation pattern is then sensitive to φ . A priori knowledge about $\Delta\delta$ is then not necessary and it can be easily

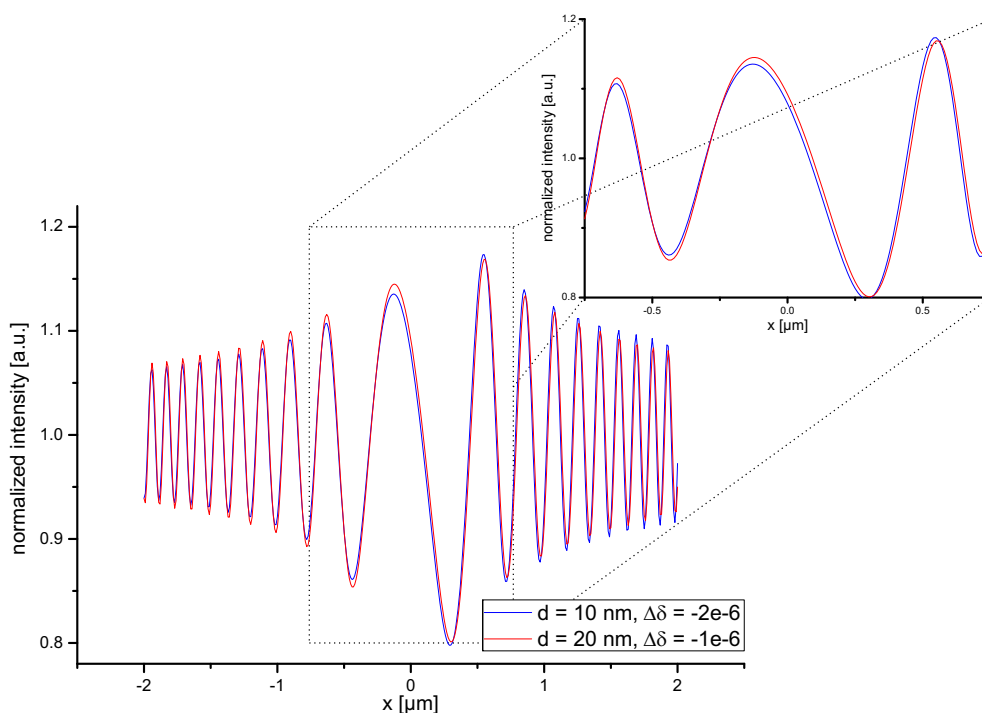


Fig. S6 Simulation of the diffraction pattern for varying values of thickness d and refractive index difference $\Delta\delta$, while keeping their product constant. By increasing $\Delta\delta$, the degeneracy in the signal is gradually lifted.

distinguished between effects of thickness and electron density contrast change. We expect that more complex models requiring more structural parameters also lead to more complex diffraction pattern, carrying more information than the simple phase slit.

5 Fit parameters for the BLM model and extension to a three box fitting model

Above we have discussed the phase slit as a simple analytic reference model for the present work. Next, we present simulations of the full model (with curvature of the BLM) with parameters tuned to the experimental values, but with systematic variations, in order to illustrate the influences of the single fit parameters on the shape of the diffraction pattern. Figure S7 shows the variation of the two main structural fit parameters (a) membrane thickness d and (b) refractive index difference $\Delta\delta$ for values varying around the experimentally measured data of a thinned membrane, see figure 2(e,f) in the main text. The amplitude increase is clearly visible, showing that thickness changes on the order of 0.5 nm can be clearly distinguished, however not independently from $\Delta\delta$ as discussed above. Figure S7(c) shows the data set fitted to the same model with two different convolution functions, namely a Gaussian and a Lorentzian, respectively. Both convolution functions give satisfactory results, with a slightly smaller χ^2 value for the Gaussian function. In the end a Gaussian convolution function was used with a controlled σ value, as justified below based on the Gaussian Shell model (GSM). Finally, we give an example of how more elaborate models can be implemented, with more structural parameters to determine the bilayer profile. At present stage, the data does not really support use of models with increased number of parameters, but in future, longer path length in the beam,

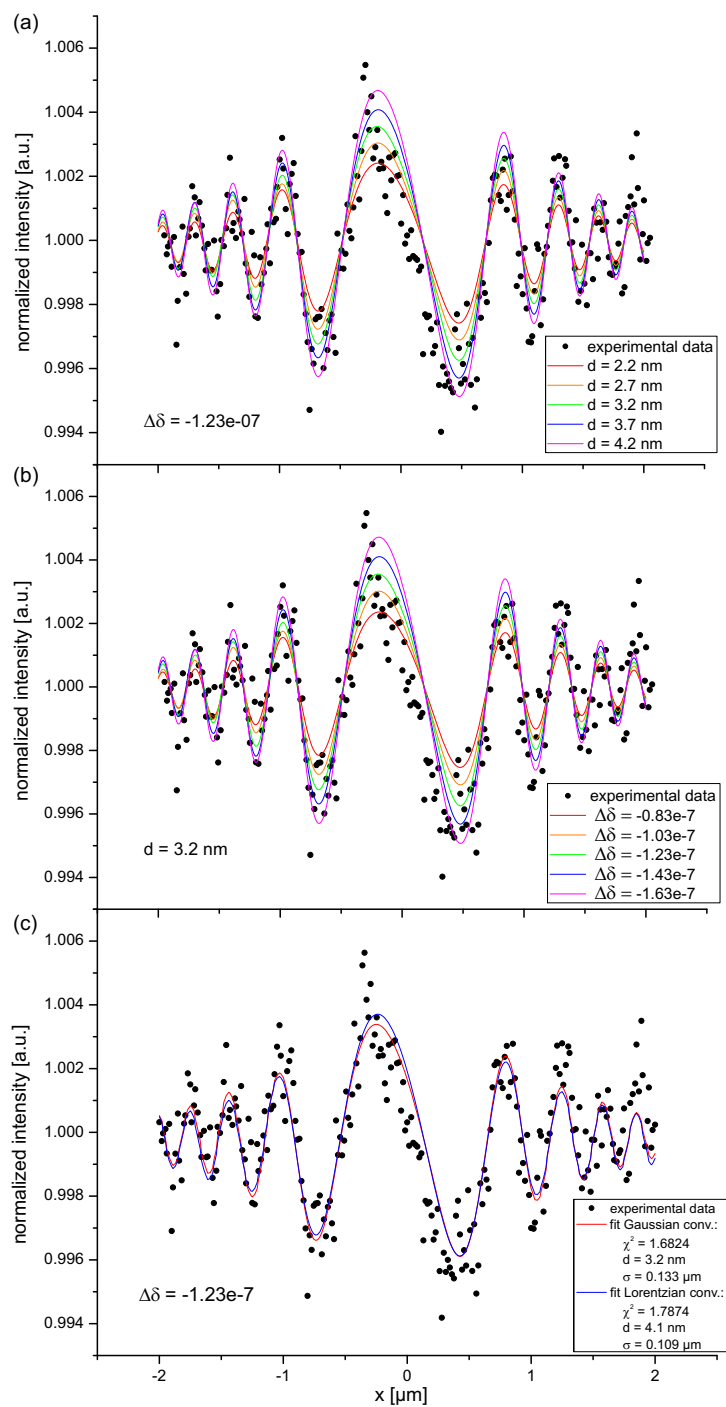


Fig. S7 The graphs show the influence of the relevant fitting parameters on the signal. Different curves for (a) thickness d and (b) refractive index difference $\Delta\delta$ have been simulated according to the experimental data set, using a single box model. Fixed parameters are: $\sigma = 0.133$ μm (Gaussian FWHM), $z = 6.8$ mm, and $R = 1.7$ mm. In (c) the comparison of two different convolution functions, Gaussian and a Lorentzian, for data fitting is shown along with the corresponding fit results.

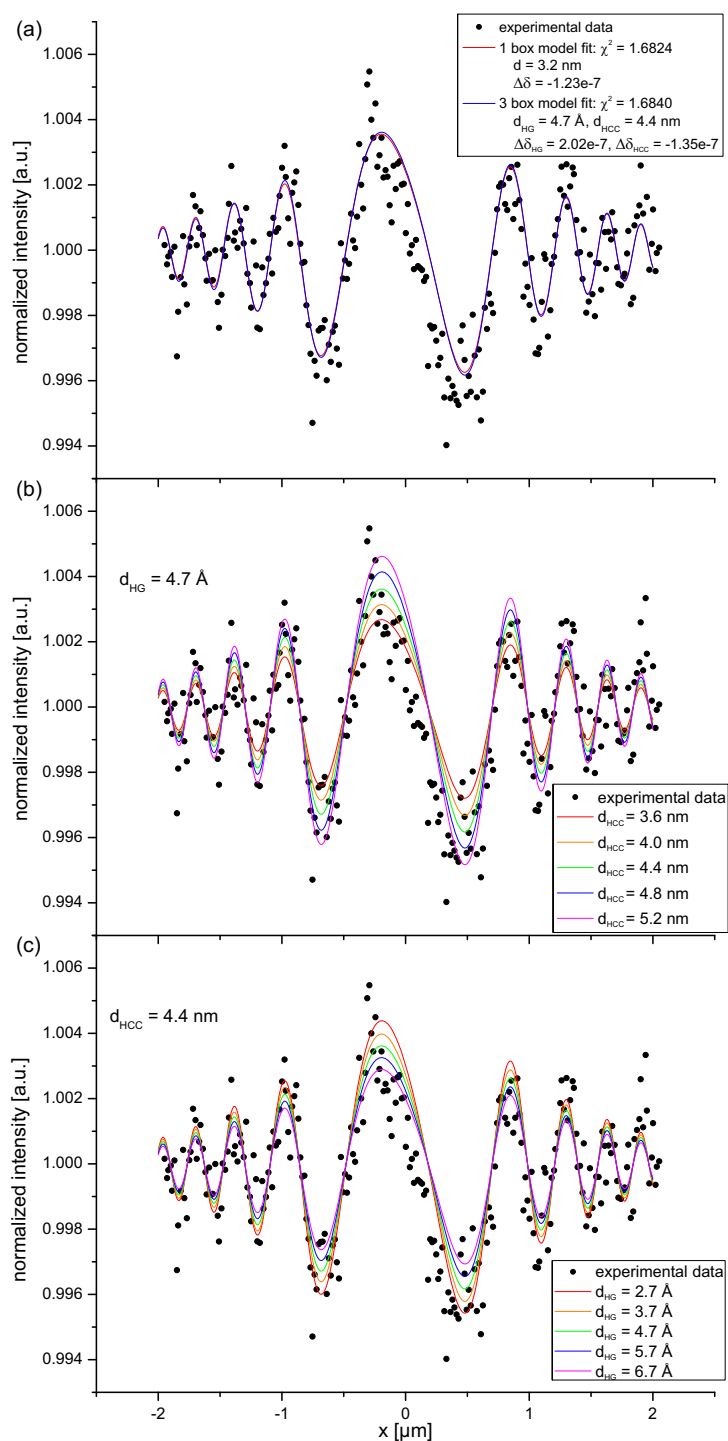


Fig. S8 The comparison of single and three box model and influences of fitting parameters. (a) The experimental data can be equally well fitted by a single box model and a model based on three boxes (headgroups - hydrocarbon chains - headgroups). (b) Influence of the hydrocarbon chain interlayer thickness and (c) of the headgroup thickness on the simulated profile. See discussion in the text. All curves have been simulated by using the following parameter values: $\sigma = 0.133$ μm (Gaussian FWHM), $z = 6.8$ mm, $R = 1.7$ mm.

lower photon energy, smaller defocus, and less wavefront aberrations may all work together to achieve better signals, allowing more detailed investigations. The obvious choice for a model beyond a simple slab of (hydrophobic) membrane thickness d is a model based on three boxes. Such a model allows for the differentiation between the hydrophilic headgroup (HG) and the hydrophobic hydrocarbon chain (HCC) regions of the bilayer, and is commonly used in x-ray reflectivity. Figure S8(a) shows that the diffraction profile of a thinned membrane can be well fitted by using the three box model yielding a fit quality comparable to that of the single box model. The (fixed) values used for $\Delta\delta$ are taken from high resolution x-ray reflectivity experiments on multilayer membrane stacks performed by our group, corresponding to electron densities of $\rho_{HG} = 0.42 e^-/\text{\AA}^3$ and $\rho_{HCC} = 0.27 e^-/\text{\AA}^3$ with respect to the surrounding water with $\rho_{H_2O} = 0.33 e^-/\text{\AA}^3$. The larger overall thickness of the three box fit results from the fact that the single box model can only represent a layer of averaged electron density with a reduced thickness. While the (fitted) headgroup thickness $d_{HG} = 4.7 \text{\AA}$ seems quite small the thickness for the hydrocarbon chain region $d_{HCC} = 4.4 \text{ nm}$ appears to be reasonable for a freestanding bilayer membrane prepared from solvent containing solutions. In figure S8(b,c) a comparison between different values of (b) d_{HCC} and (c) d_{HG} is shown. It can be seen that the increase / decrease of the amplitudes depends on the sign of the respective $\Delta\delta$. Furthermore the graphs demonstrate that even small changes in the headgroup thickness d_{HG} can be determined on the order of Angstroms. This indicates that with low noise data the presented method is powerful enough to resolve structural changes along the membrane normal much below the molecular dimension.

6 Coherence properties: Gaussian Shell model

The analysis of the Fresnel diffraction fringes requires a convolution parameter σ which can be treated as a free empirical parameter. On a more advanced level, one can model the coherence properties of the KB beam to fix this parameter to an expected value. Note that the detector point-spread-function would also lead to a convolution of the signal, but for the high magnification and high detector resolution used here, partial coherence clearly dominates the 'damping effect' of the signal.

As recently shown by Talbot interferometry, partially coherent undulator radiation focused by KB mirrors lead to an exit wavefield which can be well described by the Gaussian Shell model¹¹. According to the Gaussian-Shell model¹², and assuming quasi-monochromatic waves, the mutual intensity J for any two points in a plane orthogonal to the optical axis is given by

$$J_{1,2}(x_1, x_2) = \sqrt{I_1(x_1)I_2(x_2)} \exp(-(x_1 - x_2)^2 / (2\xi^2)), \quad (11)$$

where ξ or the FWHM equivalent $\xi_{FWHM} = 2\sqrt{2\ln 2}\xi$ can be defined as the lateral coherence length. If the coherence length in the focal plane is smaller than the focal width s (FWHM), which is the case for the present experiment, ξ_{FWHM} is dominated by free space propagation behind the focus. For distances z larger than the Rayleigh length behind the focal plane, ξ increases linearly with z

$$\xi_{FWHM} = \frac{4\ln(2)}{2\pi} \frac{\lambda z}{s}, \quad (12)$$

just as in the limiting case of an incoherent (secondary) source of width s . Thus, the measured values of $s = 133\text{nm}$ and the experimental value for z fix the coherence length in the sample plane. Under these conditions, the source width s and ξ or more precisely the spread of wave vectors corresponding to the coherent cone of the beam form a Fourier pair. Accordingly, the signal in the sample plane has to be convoluted by a Gaussian with a parameter $\sigma = s$. Here both values are taken as FWHM. In summary, coherence arguments fix the convolution parameter used in the fit, which is thus not free. The fitting was therefore carried out, when possible, with the expected value $\sigma = 0.133\mu\text{m}$ (in de-magnified coordinates, after the coordinate transformation discussed above). However, some data sets did not yield satisfactory results at this values, but needed larger σ . We attribute these deviations to vibrations (and undulations) of the membrane interface. This may lead to an additional smearing of the signal summed over the accumulation time, a noticeable effect when tension is not high enough.

7 Additional result: thinned membrane section

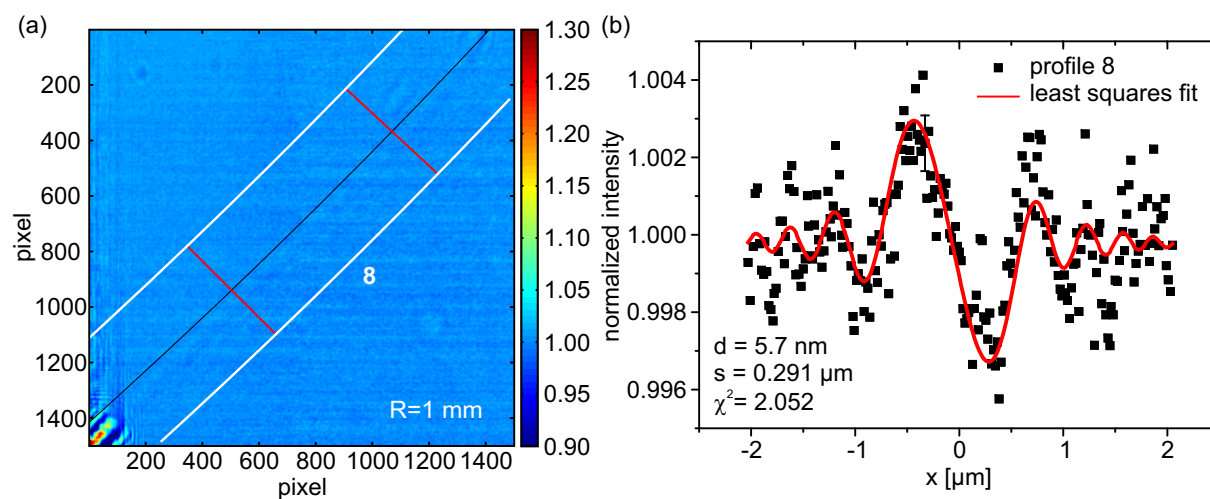


Fig. S9 (a) Image of a rather broad and straight section of completely thinned membrane, observed at another preparation than the data sets shown in the main manuscript. Image taken at parameters $z_{eff} = 7.623\text{ mm}$, $R = 1\text{ mm}$ and magnification $M = 67.99$, with (b) corresponding profile and least squares fit. Although the profile is average over 803 line cuts it shows a large noise level due to dominating mirror artifacts.

Figure S9(a, b) depicts another representative example (*profile 8*) of a thinned membrane. The image is recorded at an effective propagation distance of $z_{eff} = 7.623\text{ mm}$, corresponding to $M = 67.99$, resulting in a thickness $d = 5.7\text{ nm}$. The convolution parameter $\sigma = 0.291\ \mu\text{m}$ is relatively large compared to the previous example, resulting from the larger region of interest (ROI), which includes 803 line cuts. Such a ROI can hardly be fitted by a circle, without deviations from the membrane contour. The larger ROI is needed in this special case since mirror artifacts could not be completely eliminated after flat and dark field correction in this case. Consequently, the noise level is higher and the upper and lower errors become approximately $\pm 58\%$ of the absolute thickness values. Averaging over a larger lateral range can also result in a signal which averages over more thermal fluctuations, which also leads to a larger smearing, i.e. it would act in the same direction as a reduced coherence length. The error analysis shows that

the current limitation, apart from partial coherence and achievable defocus, is mostly limited by beam stability and residual wave front aberrations, in particular in form of mirror artifacts. These originate most probably from wavefront distortions by the mirror profile which change with drifting beam illumination, and can therefore not be completely factored out.

References

- 1 P. Müller, D. Rudin, H. Tien and W. Wescott, *Nature*, 1962, **194**, 979–980.
- 2 H. Tien and A. Ottova-Leitmannova, *Membrane Biophysics*, Elsevier Science B.V., 2000.
- 3 M. Montal and P. Mueller, *Proceedings of the National Academy of Sciences*, 1972, **69**, 3561.
- 4 A. Beerlink, P.-J. Wilbrandt, E. Ziegler, D. Carbone, T. Metzger and T. Salditt, *Langmuir*, 2008, **24**, 4952.
- 5 A. Beerlink, M. Mell, M. Tolkiehn and T. Salditt, *Applied Physics Letters*, 2009, **95**, 203703.
- 6 A. Otten, S. Köster, B. Struth, A. Snigirev and T. Pfohl, *Journal of Synchrotron Radiation*, 2005, **12**, 745.
- 7 R. Dootz, H. Evans, S. Köster and T. Pfohl, *Small*, 2007, **3**, 96.
- 8 D. Paganin, *Coherent X-Ray Optics*, Oxford University Press, 2006.
- 9 A. Beerlink, *Ph.D. thesis*, University of Göttingen, Germany, 2010.
- 10 M. Mell, *M.Sc. thesis*, University of Göttingen, 2009.
- 11 T. Salditt, S. Kalbfleisch, M. Osterhoff, S. Krüger, M. Bartels, K. Giewekemeyer, H. Neubauer and M. Sprung, *Optics Express*, 2011, **19**, 9656–9675.
- 12 I. Vartanyants and A. Singer, *New J Phys*, 2010, **12**, 035004.